Elastohydrodynamic lubrication of soft-layered rollers and tensioned webs in roll-to-plate nanoimprinting

Snieder, Jelle; Dielen, Marc; van Ostayen, Ron A.J.

Important note
To cite this publication, please use the final published version (if applicable).
Please check the document version above.

Original Article

Elastohydrodynamic lubrication of soft-layered rollers and tensioned webs in roll-to-plate nanoimprinting

Jelle Snieder[1,2] iD **, Marc Dielen[2]** iD **and Ron AJ van Ostayen[1]** iD

Abstract

This work presents the development of a numerical model for the elastohydrodynamic lubrication of roll-to-plate nano-imprinting with flexible stamps. Roll-to-plate nanoimprinting is a manufacturing method to replicate micro- and nanotextures on large-area substrates with ultraviolet-curable resins. The roller is equipped with a relatively soft elastomeric layer, which elastically deforms during the imprint process. The elastic deformation is described by linear elasticity theory. It is coupled to the pressure build-up in the liquid resin film, which is described by lubrication theory. The flexible stamp, which is treated as a tensioned web, is pre-tensioned around the roller. The elastic deformation of the tensioned web is described by the large-deflection bending of thin plates equations, considering its non-negligible bending stiffness. A Fischer–Burmeister complementarity condition captures the contact mechanics between the tensioned web and the roller. The governing equations combine in a coupled elastohydrodynamic lubrication model, which is fully described by a set of non-dimensional numbers. These are used in a parameter study to investigate the effect on the pressure and film height distributions. It is shown that the bending stiffness of the tensioned web results in an additional hydro-dynamic pressure peak and corresponding minimum in the film height, near the inlet of the roller contact. An increase of the bending stiffness corresponds to a decrease in film height. The numerical results are compared with benchmarks from literature and experimentally validated with layer height measurements from flat layer imprints. Good agreement is found between the numerical and experimental results.

Introduction

Nanoimprint Lithography (NIL) is an emerging manufacturing technology to replicate micro- and nanotextures with high resolution on rigid and flexible substrates.[1,2] The working principle is based on a moulding process, in which a stamp is pressed into a liquid resist material. The resist material is mechanically deformed to conform to the surface topography of the stamp. Ultraviolet (UV) NIL employs photo-polymerizable resins, which can quickly fill the stamp features, in combination with UV-transparent stamps.[3] After solidification of the resin by UV-light, the stamp is delaminated and a negative of the textured pattern is left on the substrate. Roller-based nanoimprinting enables an increased fabrication throughput and the possibility to pattern large-area substrates at once.[4–6] The stamps may be re-used many times, which makes roller-based NIL an interesting and versatile technology for cost-effective volume manufacturing.[7] The patterning method can be used to fabricate functional layers or to enhance the optical or mechanical properties

of a substrate. Applications can be found in, for example, anti-reflection or light-trapping films for displays and solar panels,[8,9] optical waveguides for augmented reality,[10] drag reduction films for aviation and shipping,[11,12] antifouling surfaces,[13,14] and many more.

A roller-based imprint system can be equipped with one or multiple rollers. Various configurations of the stamp, roller(s) and substrate are available and can be used to classify the different systems.[15,16] Figure 1 shows a schematic diagram of a UV-cure roll-to-plate nanoimprint system, which is considered in this study. It

[1]Department of Precision and Microsystems Engineering, Delft University of Technology, Delft, The Netherlands
[2]Morphotonics B.V., Veldhoven, The Netherlands

Corresponding author:
Jelle Snieder, Department of Precision and Microsystems Engineering, Delft University of Technology, Mekelweg 2, 2628 CD Delft, The Netherlands.
Email: j.snieder@tudelft.nl

makes use of a number of rollers to guide a flexible stamp. The rollers are equipped with a relatively soft, elastomeric layer to ensure conformal contact with the substrate. The imprint roller (middle left) presses the flexible stamp into the UV-curable resin droplets, which have been dispensed on the substrate. The resin droplets merge and spread into a thin layer. After UV-curing of the resin layer, the flexible stamp is delaminated from the substrate by the delamination roller (middle right). The final imprint consists of the preferred texture on top of a residual layer. The residual layer is ideally thin and uniform over the entire surface, in order to prevent poor optical performance of the product.[16] Moreover, the imprinted texture can optionally be transferred into the substrate material in a subsequent etching process step by utilizing the imprinted pattern as an etching mask. A thin and uniform residual layer is essential for an efficient and high quality etch.[2,17,18]

Simulation of the imprint process will allow for the improved prediction of the residual layer thickness to further improve the imprint quality. The residual layer thickness is governed by the interaction of the hydrodynamic forces in the resin and the elastic forces of the flexible stamp and the elastomeric layer around the imprint roller. The hydrodynamic pressure-build up in the liquid resin film results in elastic deformation of both the flexible stamp and the elastomeric layer. The pre-tensioned, flexible stamp exerts an additional contact pressure on part of the elastomeric layer, after which it loses contact with the roller downstream of the roller contact. The elastic deformation is relatively large compared to the film height and will affect the hydrodynamic pressure build-up, in return. This coupling is described by elastohydrodynamic lubrication (EHL) theory, which can be used to predict the residual layer thickness. Soft-layered EHL deals with the lubrication of relatively soft, elastomeric layers. The finite thickness of the elastomeric layer increases the effective stiffness of the roller

contact, which influences the pressure build-up and film height in the roller contact.[20–23]

In literature, analytical and numerical models are presented to simulate the residual layer thickness in roller-based imprint systems.[4,24,25] Moreover, when excluding the textures, roller-based imprinting shows a resemblance with forward roll coating and printing.[22,26–29] These are well-known industrial methods to apply thin liquid coatings on flexible, foil-like substrates using rubber covered rollers. EHL theory is used to determine the process dependencies on the coating or printing layer height. In all of these simulations, the influence of the elastic deformation of the flexible stamp or foil and the interaction with the rollers are not taken into account. In previous work, the development of an EHL model to predict the residual layer thickness in roll-to-plate nanoimprint systems with pre-tensioned, flexible stamps is presented.[19] It has been shown that an increase in tension of the flexible stamp, which is assumed to be perfectly flexible, results in a reduction of the residual layer thickness. The contact mechanics between the flexible stamp and the roller are a unique aspect of the roll-to-plate nanoimprint process. Moreover, the bending stiffness of the flexible stamp is not negligible and differs based on the geometry and material properties. Both contact mechanics and bending stiffness must be included in the EHL model to further improve the prediction of the residual layer thickness.

The current work presents the development of a numerical EHL model to accurately describe the physics of the roll-to-plate nanoimprint process with flexible stamps, which are treated as tensioned webs with a non-negligible bending stiffness. The study focuses on the flat layer thickness and the influence of textures is not taken into account. The numerical model is described in detail and the numerical results are experimentally validated with layer height measurements of flat layer imprints. Unique contributions of this work are the
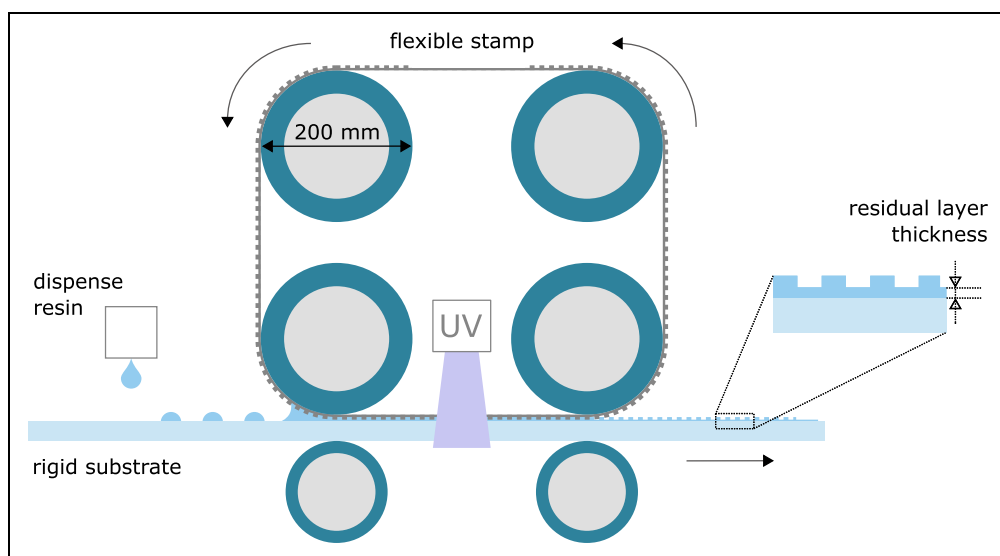

Figure 1. Reproduced with permission from.[19] Roll-to-plate nanoimprint system.

implementation of the elastic deformation and contact mechanics of tensioned webs in an EHL system, and the application of this theory in a roll-to-plate nanoimprint process. The model can be used to study the influence of the process parameters, machine parameters, and material properties on the pressure and film height distributions. Moreover, it can be used to directly assess the film thickness for a given set of process parameters. This information is useful to determine the required amount of resin for a specific imprint or to tune the process parameters for a preferred film thickness.

Methods

This section describes the set-up of the numerical EHL model, including the governing equations and the numerical implementation. Thereafter, the experimental validation method is discussed.

Model description

The numerical model is based on the full-system finite element approach for EHL problems.[30] The modelled system geometry of the imprint roller contact, which is treated as a line contact, is shown in Figure 2(a).

The imprint roller with radius R is pressed onto the rigid substrate. The roller is equipped with an elastomeric layer of thickness d. A tensioned web (i.e. flexible stamp) is partly wrapped around the imprint roller and applies a contact pressure onto the elastomeric layer. Downstream of the roller contact, the tensioned web looses contact with the roller and moves along with the substrate. The tensioned web and substrate are separated by a thin film of resin with film height h. The final film height is indicated by h_f. The lubricated roller contact is assumed to be fully flooded and is subject to an effective load F_L in vertical z-direction. The load is a combination of the externally applied roller load and web tension. The substrate and tensioned web are assumed to be smooth and are moving with a unidirectional, constant surface speed of u_1 and u_2, respectively. It is assumed that all elastic deformation occurs in the relatively compliant, elastomeric layer. As the contact width is relatively small compared to the roller radius, a simplified equivalent geometry can be used, as shown in Figure 2(b). A rigid roller with radius R is pressed onto the flat, elastomeric layer, which is unwrapped from the roller core. A new coordinate system is introduced: x' is the coordinate tangential to the roller surface and z' is the coordinate normal to the roller surface, pointing towards the rigid roller.

The model is governed by five main equations: linear elasticity equations, Reynolds equation, large-deflection bending of thin plates equations, the Fischer–Burmeister constraint function, and a load balance equation. The equations are solved together to determine the elastic deformation components u and w of the elastomeric layer, the hydrodynamic pressure p, the contact pressure p_c, the tensioned web curvature κ, and the elastic deformation of the tensioned web w_w. To ensure numerical robustness and faster convergence, the model variables are scaled. Before the governing equations are presented, the definition of the dimensionless scaling is discussed. The following dimensionless variables are used in the description of the equations:

$$
\begin{aligned}
& P = \frac{p}{p_h}, \quad P_c = \frac{p_c}{p_h} \\
& U = \frac{uR}{a_h^2}, \quad W = \frac{wR}{a_h^2}, \quad W_w = \frac{w_w R}{a_h^2} \\
& G = \frac{gR}{a_h^2}, \quad H = \frac{hR}{a_h^2}, \quad K = R\kappa \\
& X' = \frac{x'}{a_h}, \quad Z' = \frac{z'}{d}
\end{aligned}
\tag{1}
$$

with the dimensionless hydrodynamic film pressure P, tensioned web contact pressure P_c, elastic deformation components U and W, web deformation W_w, gap G, film height H, tensioned web curvature K, and spatial coordinates X' and Z'. The parameters a_h and p_h correspond to the Hertz dry contact half-width and peak pressure, respectively. They are based on the mechanical properties of the elastomeric layer:

$$
\begin{aligned}
a_h &= \sqrt{\frac{8F_L R}{\pi E'}}, \\
p_h &= \frac{2F_L}{\pi a_h},
\end{aligned}
\tag{2}
$$

where E' is the effective elastic modulus. As it is assumed that all elastic deformation occurs in the elastomeric layer, it is given by:

$$
\frac{2}{E'} = \frac{1 - \nu^2}{E},
\tag{3}
$$

where ν is the Poisson's ratio. The equations are applied on the computational domain in Figure 3, which represents the unwrapped elastomeric layer. The dimensionless scaling results in a fixed computational domain with a dimensionless length of 20 and unit dimensionless height, due to the above definition of X' and Z'. The coordinate $X' = 0$ represents the roller centre.

The dimensionless linear elasticity equations are applied on the elastomeric layer domain Ω in Figure 3. For a derivation of these scaled equations, the reader is referred to Habchi.[31] They are given by:

$$
\begin{aligned}
& \frac{\partial}{\partial X'}\left[(\lambda + 2\mu)\frac{d}{a_h}\frac{\partial U}{\partial X'} + \lambda\frac{\partial W}{\partial Z'}\right] \\
& \quad + \frac{\partial}{\partial Z'}\left[\mu\left(\frac{a_h}{d}\frac{\partial U}{\partial Z'} + \frac{\partial W}{\partial X'}\right)\right] = 0, \\
& \frac{\partial}{\partial X'}\left[\mu\left(\frac{\partial U}{\partial Z'} + \frac{d}{a_h}\frac{\partial W}{\partial X'}\right)\right] \\
& \quad + \frac{\partial}{\partial Z'}\left[\lambda\frac{\partial U}{\partial X'} + (\lambda + 2\mu)\frac{a_h}{d}\frac{\partial W}{\partial Z'}\right] = 0,
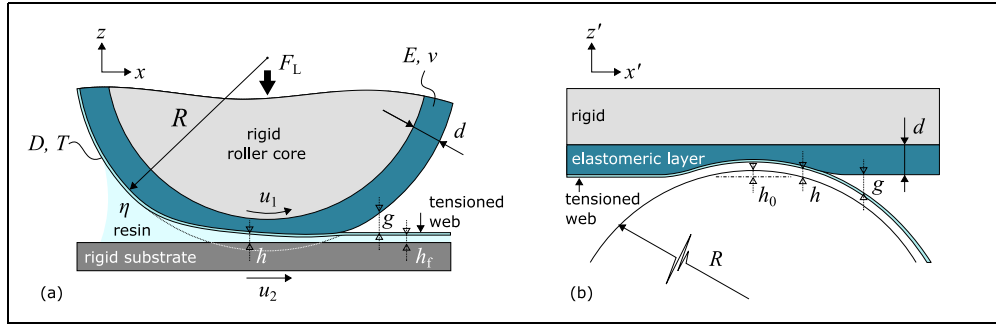\end{aligned}
\tag{4}
$$

Figure 2. Adapted with permission from Snieder et al.[19] (a) Schematic diagram of the imprint roller with tensioned web. The elastic deformation of the elastomeric layer is highly exaggerated for illustrative purposes. (b) Equivalent geometry of the imprint roller with tensioned web.

where λ and μ correspond to the Lamé parameters:

$$\lambda = \frac{\nu E_{eq}}{(1 - 2\nu)(1 + \nu)},$$
$$\mu = \frac{E_{eq}}{2(1 + \nu)}. \tag{5}$$

The parameter E_{eq} corresponds to the equivalent elastic modulus of the elastomeric layer, which is defined by:

$$E_{eq} = E \frac{a_h}{Rp_h}. \tag{6}$$

The elastic modulus is multiplied by $a_h/(Rp_h)$ to directly use the dimensionless tensioned web contact pressure P_c as a pressure load on domain boundary $\partial\Omega_C$.[32] The boundary conditions are specified as follows:

$$\begin{cases} U & = W = 0 & \text{on } \partial\Omega_T, \\ U & = 0 & \text{on } \partial\Omega_L \text{ and } \partial\Omega_R, \\ \sigma_n & = \sigma \cdot \vec{n} = \sigma_{zz} = \\ & \lambda \frac{\partial U}{\partial X} + (\lambda + 2\mu) \frac{a_h}{d} \frac{\partial W}{\partial Z} = P_c & \text{on } \Omega_C, \\ \sigma_n & = \sigma_t = 0 & \text{elsewhere.} \end{cases} \tag{7}$$

The parameters σ_n and σ_t are the normal and tangential components of the stress tensor, respectively.

The resin flow is described by lubrication theory, which assumes a constant pressure across the film thickness. The dimensionless, steady-state, incompressible Reynolds equation in one dimension is given by:[33]

$$\frac{\partial}{\partial X'}\left(-\frac{a_h^3 p_h}{12R^2\eta u_\Sigma}H^3\frac{\partial P}{\partial X'} + \frac{H}{2}\right) = 0, \tag{8}$$

where η is the dynamic viscosity of the resin, and u_Σ is the sum of the top and bottom surface velocity u_1 and u_2, respectively. The Reynolds equation assumes Newtonian fluid behaviour and isothermal conditions. The validity of these assumptions is confirmed by viscosity measurements and monitoring of the roller temperature. Equation (8) is applied on domain $\partial\Omega_H$ in Figure 3. It is defined by $-4.5 \leq X' \leq 10$, which is sufficiently wide to capture the pressure build-up in the thin film of resin.[30] Zero pressure boundary conditions are applied on the edges of the domain. The hydrodynamic

film pressure P is determined for a given film height distribution H:

$$H(X') = H_0 + H_w + W_w(X'),$$
$$H_w = \begin{cases} \frac{X'^2}{2} & \text{for } X' \leq 0, \\ 0 & \text{for } X' > 0. \end{cases} \tag{9}$$

where H_0 is the unknown rigid body displacement. A negative value indicates roller engagement, as shown in Figure 2(b). The second term H_w describes the initial web shape, which partly follows the roller surface. The last term $W_w(X')$ represents the web deformation, which will follow from equation (11). It is assumed that the resin can sustain small negative pressures without cavitating. Downstream of the roller contact zone, the resin is trapped between the tensioned web and the substrate. Due to the absence of a diverging roller surface, which is typically present in conventional EHL problems,[34] the presence of negative pressures will be minimum.

The tensioned web is a relatively thin plate with a non-negligible bending stiffness, and, therefore, the Föppl–von Kármán equations can be applied to describe the deformation of the web under tension and pressure.[35,36] These equations are based on the extended theory for small deflections of thin plates, by taking into account the in-plane membrane stresses, and they describe the large-deflection bending of thin plates. In the case of an infinite line contact and by assuming a constant web tension, the dimensionless stress balance in normal direction is given by:

$$\left(-\frac{D}{a_h^2 p_h R}\right)\frac{\partial^2 K}{\partial X'^2} + \left(\frac{T}{p_h R}\right)K + P_n = 0. \tag{10}$$

where D is the bending stiffness of the web and T is the web tension. The normal stress P_n is equal to the difference of the hydrodynamic film pressure and the tensioned web contact pressure; $P_n = P - P_c$. The web curvature K is approximated by the second spatial derivative of the web shape, which is described by the last two terms in
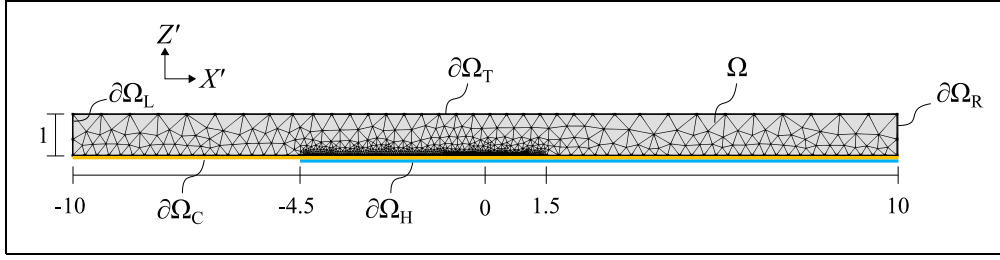
Figure 3. Adapted with permission from Snieder et al.[19] Dimensionless computational domain and mesh. The contact domain Ω_C (yellow) extends over the entire domain length ($-10 \leq X' \leq 10$), while the hydrodynamic domain Ω_H (blue) extends over part of the domain length ($-4.5 \leq X' \leq 10$).

equation (9):

$$K = \frac{\partial^2}{\partial X'^2}\left(H_w + W_w(X')\right)$$

$$= \begin{cases} 1 + \frac{\partial^2 W_w}{\partial X'^2} & \text{for } X' \leq 0, \\ \frac{\partial^2 W_w}{\partial X'^2} & \text{for } X' > 0. \end{cases} \tag{11}$$

The bending stiffness of the tensioned web is a function of the elastic modulus E_w, web thickness t and Poisson's ratio ν_w of the tensioned web:

$$D = \frac{E_w t^3}{12\left(1 - \nu_w^2\right)} \tag{12}$$

Equations (10) and (11) are applied on domain $\partial\Omega_C$ in equation (3).

The contact mechanics between the roller and tensioned web are described by two variables; the contact pressure P_c and the gap between the roller and the tensioned web G. The contact pressure P_c can be traced back to equation (10). The dimensionless gap is defined by:

$$G = G_0 + W - W_w,$$

$$G_0 = \begin{cases} 0 & \text{for } X' \leq 0, \\ \frac{X'^2}{2} & \text{for } X' > 0. \end{cases} \tag{13}$$

in which G_0 is the initial gap between the roller and the tensioned web, and W and W_w are the elastomeric layer and web deformation, respectively. The initial gap is equal to zero at the locations where the tensioned web and roller are initially in contact, and increases with the approximated roller shape from the location where the tensioned web and roller lose contact at $X' = 0$. In general, two different regions can be identified: a contact region in which the contact pressure is unknown (but larger than 0) and the gap is known (namely 0), and a region without contact where the contact pressure is known (namely 0) and the gap is unknown. This reasoning can be captured in a complementarity condition:

$$\begin{aligned} P_c \geq 0 \quad \text{and} \quad G = 0, \\ P_c = 0 \quad \text{and} \quad G \geq 0. \end{aligned} \tag{14}$$

The complementarity condition of the contact problem is satisfied by adding a modified constraint function to

domain Ω_C in the model, known as the Fischer–Burmeister function:[37]

$$P_c + G - \sqrt{P_c^2 + G^2} = 0. \tag{15}$$

This function is often used in (elasto)hydrodynamic lubrication models as a mass-conserving cavitation algorithm,[19,38] with the film pressure and the mass fraction as dependent variables. In the present study, the Fischer–Burmeister function will reveal the occurrence of contact between the tensioned web and the roller.

The load equilibrium is derived by balancing the pressure force from the hydrodynamic film pressure build-up with the effective roller load per unit length:

$$\int_{\Omega_H} P \, dX' = \frac{\pi}{2}. \tag{16}$$

The right side of this equation relates to the Hertz scaling from equation (2). The equation is satisfied by regulating the gap H_0 in equation (9), which is one of the unknowns in the system of equations.

Numerical implementation

The elastohydrodynamic model is composed of the linear elasticity equations in equation (4), the Reynolds equation in equation (8), the large-deflection bending of plates equations in equations (10) and (11), the Fischer–Burmeister function in equation (15), and the load balance equation in equation (16). The equations are implemented in the finite element method (FEM) software package COMSOL Multiphysics®.[39] A second-order (quadratic) discretization is employed for the Reynolds equation, the large-deflection bending of plates equations and the Fischer–Burmeister constraint function. The linear elasticity equations are discretized with third-order (cubic) elements, to ensure a smooth second-order derivative of the web curvature in equation (11). The use of FEM allows for unstructured meshing of the computational domain in Figure 3. The domain Ω is built with a coarse triangular mesh, while the mesh is refined at the lower boundary $\partial\Omega_C$, on which the mesh size varies. A relatively coarse mesh is used on the outer parts ($-10 \leq X' \leq -4.5$ and $1.5 \leq X' \leq 10$), while the mesh size is fine in the outer regions of the roller contact ($-4.5 \leq X' \leq -1$ and $1 \leq X' \leq 10$), finer in the central

region of the roller contact $(-1 \leq X' \leq 0.5)$, and finest in the last region of the roller contact $(0.5 \leq X' \leq 1)$. These settings have been confirmed by mesh convergence studies.

The starting point of the numerical procedure is the selection of a set of appropriate initial values for the variables as listed in equation (1). The initial hydrodynamic pressure distribution is equal to the Hertz dry contact pressure:

$$P = \begin{cases} \sqrt{(1 - X'^2)} & \text{for } -1 \leq X' \leq 1, \\ 0 & \text{elsewhere.} \end{cases} \quad (17)$$

The initial guess for the elastic deformation components U and W is equal to the elastic deformation corresponding to the Hertz dry contact pressure. The initial contact pressure is equal to the sum of the Hertz dry contact pressure and the contact pressure from the tensioned web on the locations where the web and roller are initially in contact:

$$P_c = \begin{cases} \frac{T}{p_h R} + \sqrt{(1 - X'^2)} & \text{for } X' \leq 0, \\ 0 & \text{for } X' > 0. \end{cases} \quad (18)$$

The gap between the roller and tensioned web G is initialized with the initial gap G_0. The initial curvature of the tensioned web is equal to the dimensionless roller curvature of 1 for $X' \leq 0$ and equal to zero for $X' > 0$. The initial elastic deformation of the tensioned web W_w is set to zero. The Fischer–Burmeister complementarity function will directly ensure that the tensioned web follows the roller shape wherever the initial gap is equal to zero. Lastly, the initial constant gap H_0 is set to a small positive number (e.g. ~ 0.01). Starting from the initial values, the system of equations is iteratively solved to find the hydrodynamic pressure P, contact pressure P_c, film height H, elastic deformation components U and W, tensioned web curvature K, and tensioned web deformation W_w. This is done in a fully coupled manner until convergence is reached. The final film height H_f is

Figure 4. Morphotonics Portis NIL1100 roll-to-plate nano-imprint equipment.[41]

determined by evaluating the film height at the end of the hydrodynamic domain $\partial\Omega_H$ at $X' = 10$.

Experimental

The numerical model is validated with multiple flat layer imprints, which have been produced on the Morphotonics Portis NIL1100 roll-to-plate nanoimprint tool in Figure 4. The imprints are fabricated using flexible, transparent stamps, which do not contain any textures. The stamps are given an anti-adhesive treatment to ensure a smooth delamination from the UV-cured resin layer. They are pretensioned around test rollers, which are equipped with a 7.5 mm thick elastomeric layer. It has an effective elastic modulus of 3.2 MPa and a Poisson ratio of 0.47. Elastomers are known for their viscoelastic material behaviour. The viscoelasticity can be quantified by the dimensionless Deborah number, which represents the ratio between the material relaxation time and the process time. The linear elastic behaviour of the elastomeric layer is confirmed by compression tests. The combination of a relatively high relaxation time (~ 14 s) and a relatively low process time (~ 0.35–3.1 s) results in a relatively high Deborah number (~ 4.5– 40). This justifies the use of a linear elastic material model with an effective elastic modulus.[40] Each imprint is performed on a 0.5 mm thick glass substrate with dimensions of 150 mm× 150 mm. The substrates are placed on a stiff carrier plate during the imprint process. To improve the adhesion between the resin and the glass substrates, the latter are cleaned with isopropyl alcohol and pretreated with an atmospheric pressure oxygen plasma and a primer containing an adhesion promoter. The average thickness of each imprinted layer is determined by optically measuring the step height of multiple small scratches fabricated in the cured imprint layer. These measurements are performed on a Keyence VK-X1100 laser confocal microscope.

The experimental validation consists of three different measurement datasets. In each dataset, different imprint parameters are varied. The first two datasets originate from previous work.[19] The experimental results are reused in this study. These imprints are performed for a variation of imprint velocity and imprint load and various in-house-developed resins are used. The viscosities and volumetric shrinkage ratios of these acrylate-based resins are shown in Table 1. Additionally, a third measurement dataset is generated. The imprints in this

Table 1. Properties of the imprint resins. The viscosities are measured at 25 °C.

Resin	Viscosity (mPa s)	Shrinkage (%)
A	6.3	12.5
B	38	8.1
C	89	9.0
D	134	7.2
E	181	8.8
F	349	7.8

Table 2. Calculated bending stiffness of the tensioned webs.

Tensioned web	Bending stiffness (Nm)
A	0.0057
B	0.0223
C	0.0823

dataset are performed with multiple tensioned webs and a variation of imprint velocity. Each web has a different bending stiffness, as shown in Table 2. Finally, the measured layer heights are converted to the liquid, pre-cured film heights using the volumetric shrinkage values in Table 1, before comparing them to the simulated film heights.

Results

This section presents the numerical and experimental results. First, the numerical model will be benchmarked to numerical results from literature. Next, a parameter study will be performed to show the impact of the various parameters in the numerical model. Lastly, the numerical model is validated by experimental results. The results are presented for a minimal set of independent, non-dimensional numbers, which fully describe the EHL problem. These are the non-dimensional modified load number $\overline{M}$, elastomeric layer thickness number $\overline{d}$, bending stiffness number $\overline{D}$, web tension number $\overline{T}$, and Poisson's ratio ν:

$$\overline{M} = \overline{W}\left(2\overline{U}\right)^{-\frac{1}{2}},$$

$$\overline{d} = \frac{d}{a_{\mathrm{h}}},$$

$$\overline{D} = \frac{D}{a_{\mathrm{h}}^2 p_{\mathrm{h}} R}, \tag{19}$$

$$\overline{T} = \frac{T}{p_{\mathrm{h}} R},$$

$$\nu.$$

The modified load number $\overline{M}$ is composed of the non-dimensional load number $\overline{W}$ and speed number $\overline{U}$, which are given by:[42,43]

$$\overline{W} = \frac{F_{\mathrm{L}}}{E'R},$$

$$\overline{U} = \frac{\eta u_{\Sigma}}{2E'R}. \tag{20}$$

The non-dimensional numbers $\overline{d}$, $\overline{D}$, and $\overline{T}$ can be traced back to equations (4) and (10), respectively. In contrast to the infinite plane EHL problems, the elastic modulus E and Poisson's ratio ν cannot be fully combined in a reduced number E' for soft-layered contacts.[22] Therefore, the Poisson's ratio ν is a part of the non-dimensional numbers. It represents the effect of the compressibility of the elastomeric layer.
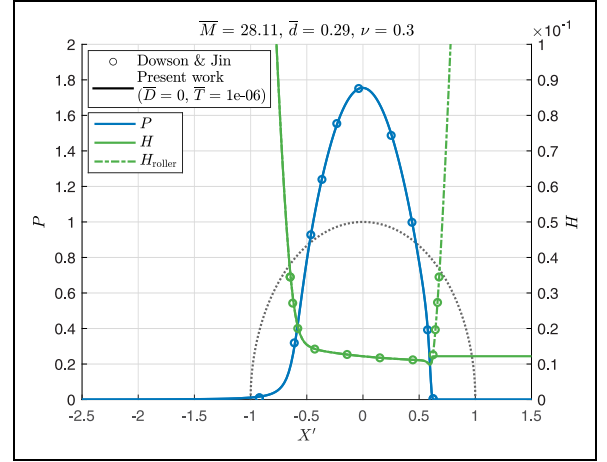

Figure 5. Comparison of the present work with results Dowson and Jin.[21] The Hertz dry contact pressure is included for reference (black dotted line).
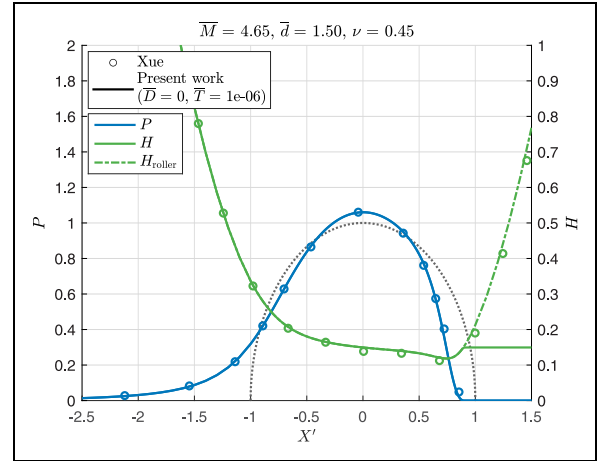

Figure 6. Comparison of the present work with results Xue.[22] The Hertz dry contact pressure is included for reference (black dotted line).

Benchmark validation

The numerical EHL model is benchmarked to results from literature for soft-layered EHL problems without a tensioned web. For this benchmark validation, the influence of the tensioned web in the present work is minimized by setting the bending stiffness number $\overline{D}$ to zero and the web tension number $\overline{T}$ to a very low value of 1×10^{-6}. The comparison between the present work and the results from Dowson and Jin and Xue are shown in Figures 5 and 6, respectively.[21,22] The graphs show the hydrodynamic film pressure P and film height H for a specific set of the non-dimensional numbers $\overline{M}$, $\overline{d}$, and ν. The Hertz dry contact pressure and roller height profile are included for a reference. The hydrodynamic film pressure smoothly increases up to a maximum at approximately the centre of the roller contact, after which it decreases. The film height quickly decreases due to the converging roller surface. A more uniform, slowly decreasing film height is shown within the roller contact zone while the

Table 3. Input parameters used for the parameter study.

Parameter	Value	Unit
F_L	2000	N/m
η	100	mPa s
R	100	mm
E	3	MPa
u_Σ	21.2	mm/s
d	9.9	mm
D	0.01	Nm
T	464.3	N/m
a_h	8.23	mm
p_h	0.16	MPa
$\overline{M}$	50	–
$\overline{d}$	1.2	–
$\overline{D}$	0.01	–
$\overline{T}$	0.03	–
ν	0.45	–

minimum film height can be found near the outlet of the roller contact. In contrast to results from literature, in the present work the film height does not diverge downstream the outlet of the roller contact. The tensioned web looses contact with the roller and the film height reaches a constant value. It is interesting to note that this behaviour in the outlet region shows a resemblance with a starved EHL contact, where only part of the gap between the two surfaces in the cavitated zone is filled. A fractional film content is introduced, which represents the film height as a fraction of the diverging roller surface.[44] The film height in the current problem follows the same trend and remains constant. Despite the differences in modelling approaches, good agreement with results from literature is found for the results obtained within the current work. This confirms the basis of the present EHL model.

Parameter study

The starting point of the parameter study is the set of input parameters in Table 3, which are typical for a roll-to-plate nanoimprint system. The parameters result in a set of non-dimensional numbers $\overline{M}$, $\overline{d}$, $\overline{D}$, $\overline{T}$, and ν.

Before the parameter study is presented, the influence of the web tension and bending stiffness of the tensioned web will be illustrated. Figure 7 shows the pressure distributions for varying values of $\overline{D}$ and $\overline{T}$. The corresponding film height distributions are shown in Figure 8. For a bending stiffness number of zero and a small web tension number, the pressure and film height distributions are qualitatively similar to the benchmark results in Figures 5 and 6. The hydrodynamic pressure profile differs from the Hertz dry contact pressure due to the finite thickness of the elastomeric layer. Moreover, the hydrodynamic pressure and contact pressure are overlapping, due to the lack of web tension and bending stiffness. The film height shows a slowly decreasing profile in the contact zone, with the minimum film height near the outlet. The tensioned web looses contact with the roller once the contact pressure is equal to zero.
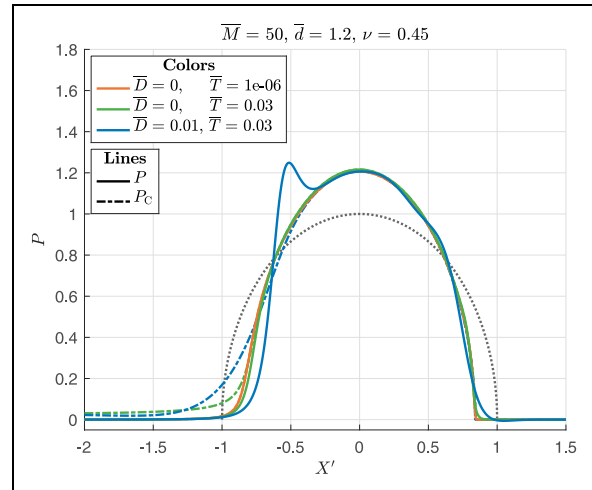

Figure 7. Hydrodynamic and contact pressure distributions for a varying web tension and bending stiffness number. The Hertz dry contact pressure is included for reference (black dotted line).
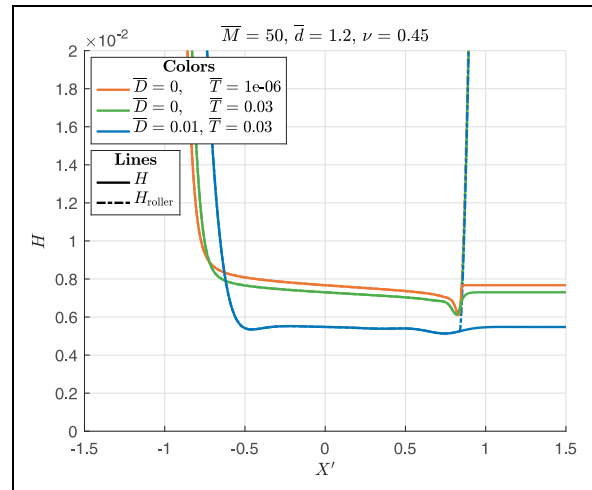

Figure 8. Film height distribution for a varying web tension and bending stiffness number.

An increase in the web tension number results in a small change in the pressure and film height distribution. In this case, the tensioned web is still considered to be perfectly flexible. It exerts an additional pressure onto the elastomeric layer material, which results in a slightly reduced contact width and film height. The hydrodynamic pressure and contact pressure are no longer overlapping. A uniform contact pressure equal to $\overline{T}$ is found in front of the roller contact, where the hydrodynamic pressure is negligibly small and the web curvature is constant.

The results become different once the bending stiffness is included. The tensioned web with bending stiffness hinders the elastic deformation of the elastomeric layer and increases the effective stiffness of the roller contact. This results in a reduced contact width and film height distribution in Figure 8 and variations in the pressure distributions in Figure 7. The difference between the hydrodynamic pressure and contact pressure is enlarged
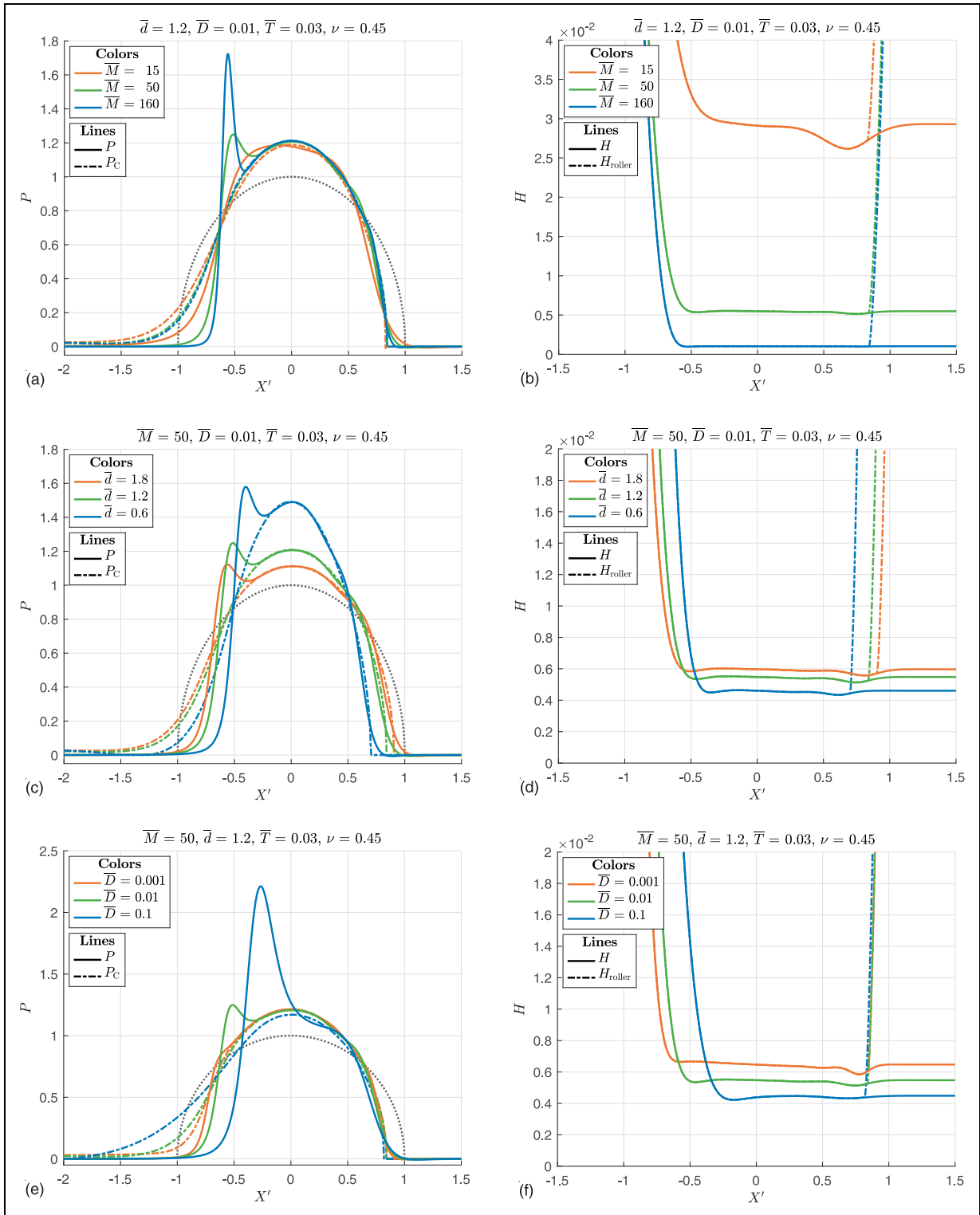
Figure 9. The figures show the hydrodynamic and contact pressure distributions (left column) and corresponding film height distribution (right column) for a variation of the non-dimensional modified load number $\overline{M}$ (top row), elastomeric layer thickness number $\overline{d}$ (middle row) and bending stiffness number $\overline{D}$ (bottom row). The Hertz dry contact pressure is included for reference (black dotted line).

as well. The impact of web tension and bending stiffness is most severe near the inlet and outlet of the roller contact, where the highest web curvature and the highest web curvature gradients are found. These are relatively small in the centre, where the roller surface is flattened. Just before the inlet of the contact, around the location of maximum curvature at $X' = -1$, the contact pressure is increased compared to the situation without bending stiffness. The combination of the bending stiffness and the increased contact pressure results in
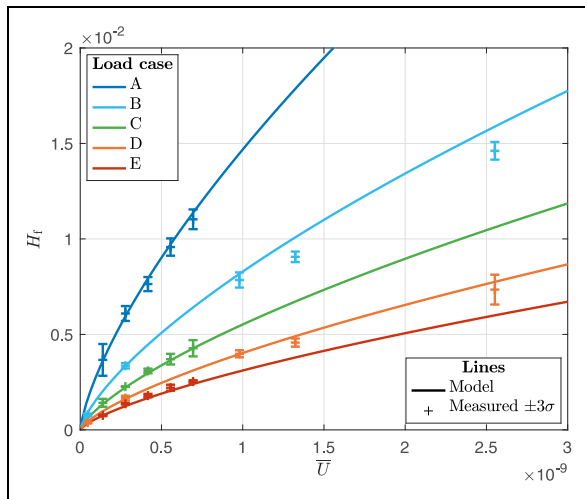
Figure 10. Numerical and experimental film heights for a variation of the load case and non-dimensional speed number $\overline{U}$. A specification of the load cases and the corresponding non-dimensional numbers can be found in Table 4.

Table 4. Specification of the load cases in Figure 10 and the corresponding non-dimensional numbers.

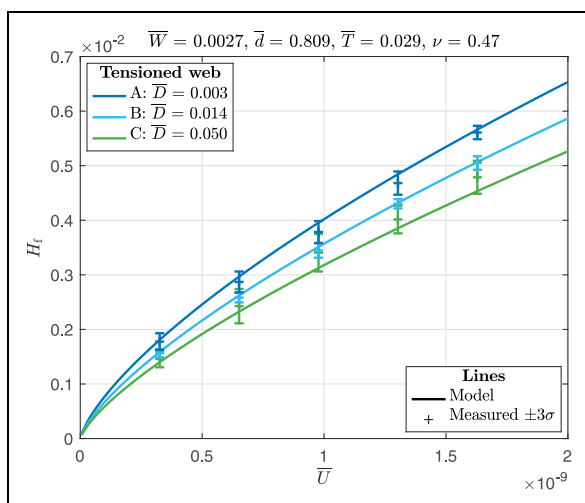| Load case	F_L (N/m)	$\overline{W}$	$\overline{d}$	$\overline{D}$	$\overline{T}$	ν
A	1000	0.0011	1.2786	0.0138	0.0307	0.47
B	1500	0.0016	1.0439	0.0075	0.0251	0.47
C	2000	0.0022	0.9041	0.0049	0.0217	0.47
D	2500	0.0027	0.8086	0.0035	0.0194	0.47
E	3000	0.0033	0.7382	0.0027	0.0177	0.47

Figure 11. Numerical and experimental film heights for a variation of the non-dimensional bending stiffness number $\overline{D}$ and speed number $\overline{U}$.

deformation of the tensioned web in other locations. Far from the inlet, around $X' = -1.5$, the contact pressure is reduced due to this deformation. The tensioned web and roller are still in contact as the contact pressure is

larger than zero. It can also be observed that the contact pressure approaches the value of $\overline{T}$ further upstream. Deformation of the tensioned web also occurs more downstream, around $X' = -0.5$. The tensioned web deforms towards the substrate surface, hereby decreasing the film height. The inlet film constriction, which is clearly visible at the inlet in Figure 8, corresponds to an additional hydrodynamic pressure peak left of the central pressure peak. This second peak is found at the location of the maximum value of the second order derivative of the web curvature. Due to the increase in hydrodynamic pressure, which is applied onto the tensioned web from below, the resulting contact pressure does not vary too much at this location. The argument that the additional hydrodynamic pressure peak and corresponding inlet film constriction are caused by the bending stiffness of the tensioned web is supported by the fact that a similar trend is observed in viscoelastic HL (VEHL).[40] Here, the hydrodynamic pressure peak and inlet film constriction are a result of the larger rigidity of the material entering the contact. At the outlet of the contact a different phenomenon can be observed. The tensioned web with bending stiffness is not able to follow the sharp curvatures of the elastomeric layer and effectively flattens the minimum film height. A slightly negative hydrodynamic pressure can be observed around $X' = 1$, due to the deformation of the tensioned web with bending stiffness, which does not directly obtain a stationary film height downstream of the roller contact. The final roller height profile appears to be remarkably symmetric, with a minimum film height near the inlet and outlet and a relatively uniform and constant film height in between.

The non-dimensional numbers are used to sweep through the solution space in an effective manner. Initial numerical experiments have shown that a variation of the non-dimensional numbers $\overline{T}$ and ν has a minor impact on the pressure and film height distribution. The results for a variation in these numbers can be found in the Supplemental Materials. The non-dimensional numbers $\overline{M}$, $\overline{d}$, and $\overline{D}$ are varied by changing the sum of the velocities u_Σ, the elastomeric layer thickness d, and the bending stiffness D, respectively. Each non-dimensional number is increased and decreased with respect to its reference value in Table 3, while the other non-dimensional numbers are kept constant. The results are shown in Figure 9. Note that the reference solution is equal to the solution for $\overline{D} = 0.01$ and $\overline{T} = 0.03$ in Figures 7 and 8.

Figure 9(a) and (b) shows the pressure and film height distributions for a variation of the non-dimensional modified load number $\overline{M}$. A decrease of $\overline{M}$ results in a reduction of the web curvature near the inlet and outlet and a less pronounced influence of the tensioned web with bending stiffness. The contact pressure does show an increase near the inlet of the roller contact, which is a result of the increased hydrodynamic pressure. This is a typical result for lightly loaded EHL contacts.[20] The corresponding film height distribution is increased and a minimum film height near the outlet is still present. The

situation is opposite for an increase of $\overline{M}$, which corresponds to a highly loaded EHL contact. The increased web curvature near the inlet results in a sharp hydrodynamic pressure peak and a corresponding inlet film constriction. The film height distribution is decreased and flattened compared to the reference solution.

The influence of a variation of the non-dimensional elastomeric layer thickness number $\overline{d}$ corresponds to soft-layered EHL results from literature.[20–22] The pressure and film height distributions are presented in Figure 9(c) and (d), respectively. An increase of $\overline{d}$ results in a larger contact width, a decreased hydrodynamic pressure, and an increased film height distribution. On the contrary, a decrease of $\overline{d}$ corresponds to a reduced contact width, an increased hydrodynamic pressure, and a decreased film height distribution. It is interesting to note that for $\overline{d} = 0.6$, the contact pressure near the inlet is equal to zero for a short distance. The gap between the roller and tensioned web is larger than zero at this location, which means that they are not in contact. This can be explained by the elastic deformation of the tensioned web, which is not able to exactly follow the roller shape. The roller height profiles in Figure 9(d) all show an approximately symmetric shape.

The results for a variation in the non-dimensional bending stiffness number $\overline{D}$ are shown in Figure 9(e) and (f). When the bending stiffness number is decreased to 0.001, the hydrodynamic pressure distribution and the contact pressure distribution approach the solution for $\overline{D} = 0$ and $\overline{T} = 0.03$ in Figure 7. The influence of the low bending stiffness number on the pressure and film height distributions is minor. An increase of $\overline{D}$ gives a large change in the pressure and film height distributions. The high bending stiffness of the tensioned web results in a strong increase of both the contact pressure near the inlet and the hydrodynamic pressure peak, which is also shifted towards the roller centre. The corresponding film height distribution is decreased and the contact width is reduced.

Experimental validation

The numerical EHL model is validated with experimental results. To clearly distinguish the film heights for various imprint parameters, the results are shown for a variation of the non-dimensional speed number $\overline{U}$, as described in equation (20). Note that the measured layer heights are converted to the liquid, pre-cured film height using the volumetric shrinkage values in equation (1).

Figure 10 shows the numerical and experimental results for a variation of the load case and the non-dimensional speed number $\overline{U}$. Each load case represents a different imprint load and results in a variation of the non-dimensional numbers $\overline{W}$, $\overline{d}$, $\overline{D}$, and $\overline{T}$, which are listed in Table 4. All results are generated with tensioned web A from Table 2 and a web tension of 370 N/m. The film heights for each load case are determined for a variation of the imprint velocity or resin viscosity. The film heights for load cases A, C, and E arise from flat layer imprints, which are fabricated with Resin B from

Table 1 (viscosity of 38 mPas) and a varying imprint velocity. The experimental results for load cases B and D correspond to a constant imprint velocity of 6.7 mm/s and a variation of the resin viscosity, as listed in Table 1. All resins are used except for Resin C. The film heights increase for an increasing speed number $\overline{U}$ and a decreasing load F_L. Good agreement is found between the results from the numerical model and the experiment.

The numerical and experimental results for a variation of the non-dimensional bending stiffness number $\overline{D}$ and non-dimensional speed number $\overline{U}$ are shown in Figure 11. The bending stiffness numbers correspond to the different tensioned webs in Table 2. A web tension of 555 N/m and an imprint load of 2500 N/m are used in both model and experiment. The film heights for each bending stiffness number are determined for a constant viscosity and a variation of the imprint velocity. The imprints are fabricated with Resin C from Table 1 (viscosity of 89 mPa s). The simulated and measured film heights increase for an increasing speed number $\overline{U}$, similar to the results in Figure 10. It can also be noticed that the film height decreases for an increasing bending stiffness number D. The simulated and measured film heights agree well.

Discussion and conclusions

In this work, a numerical EHL model is developed to describe the elastohydrodynamic lubrication in roll-to-plate nanoimprinting. The model is a multiphysics simulation with a set of coupled equations to describe the elastic deformation of the elastomeric layer, the pressure build-up in the thin film of resin, the elastic deformation of the tensioned web, and the contact mechanics between the tensioned web and the roller. The numerical results with zero bending stiffness and negligible web tension agree well with benchmark results for soft-layered EHL problems from literature, which confirms the validity of the basis of the current model approach.

The EHL problem is described by the set of non-dimensional numbers $\overline{M}$, $\overline{d}$, $\overline{D}$, $\overline{T}$, and ν. These are used in a parameter study to investigate the influence of the various process parameters. The results show that web tension has a minor effect on the pressure distribution and film height distribution. On the other hand, the bending stiffness of the tensioned web does have a significant impact. It results in an additional hydrodynamic pressure peak and corresponding inlet film constriction left of the roller centre. Moreover, it effectively flattens the film height distribution, which also decreases in magnitude. The impact of the tensioned web with bending stiffness becomes more severe when the web curvature or bending stiffness is increased. It results in an increase of the additional hydrodynamic pressure peak and a further reduction of the film height distribution. The effect of the tensioned web with bending stiffness does not significantly change when the elastomeric layer thickness is

varied. A decrease of the elastomeric layer thickness will result in an increased pressure distribution and decreased film height distribution. The numerical model is validated by experimental results for a wide range of the non-dimensional numbers. Good agreement is found between the numerical results and experimental results.

The present results contribute to a better understanding of the elastohydrodynamic lubrication of soft-layered rollers and tensioned webs in roll-to-plate nanoimprinting. The developed model can be used in the optimisation of a roll-to-plate imprint system for achieving a thin and uniform film height. Moreover, it can directly be used to determine the film height as a function of the process parameters, machine parameters, and material properties. This information can help in optimising the required amount of dispensed resin for a specific imprint or in tuning the process parameters for realising a desired film height. The simulated film heights can be converted to the cured flat layer thickness by taking into account the volumetric shrinkage ratio of the UV-curable resin. The present study is focused on the application of roll-to-plate nanoimprinting, but the model may be useful for the analysis of any EHL process which involves tensioned webs or foils, such as forward roll coating of flexible substrates or printing of paper.

ORCID iDs

Jelle Snieder https://orcid.org/0000-0001-7820-6840
Marc Dielen https://orcid.org/0000-0002-0848-3874
Ron AJ van Ostayen https://orcid.org/0000-0002-4814-544X

Supplemental Material

The supplemental material is available online at https://journals.sagepub.com/home/pij/10.1177/13506501231183860

References

1. Chou S, Krauss P and Renstrom P. Imprint of sub-25 nm vias and trenches in polymers. *Appl Phys Lett* 1995; 67: 3114–3116.
2. Schift H and Kristensen A. Nanoimprint Lithography. In Bhushan B (ed.) *Springer Handbook of Nanotechnology.* Springer Handbooks, Berlin, Heidelberg: Springer. ISBN 978-3-540-29857-1, 2007. pp. 239–278. DOI:10.1007/978-3-540-29857-1_8.
3. Haisma J, Verheijen M, van den Heuvel K et al. Mold-assisted nanolithography: a process for reliable pattern replication. *J Vac Sci Technol B: Microelectron Nanometer Struct Proce, Meas, Phenom* 1996; 14: 4124–4128.
4. Ahn SH and Guo LJ. Large-area roll-to-roll and roll-to-plate nanoimprinting lithography: a step toward high-throughput application of continuous nanoimprinting. *ACS Nano* 2009; 3: 2304–2310.
5. Kooy N, Mohamed K, Pin LT et al. A review of roll-to-roll nanoimprint lithography. *Nanoscale Res Lett* 2014; 9: 1–13.
6. Lan H. Large-Area Nanoimprint Lithography and Applications. In *Micro/Nanolithography – A Heuristic Aspect on the Enduring Technology*. London: IntechOpen, 2018. pp. 43–68.
7. Tahir U, Shim Y, Kamran M et al. Nanofabrication techniques: challenges and future prospects. *J Nanosci Nanotechnol* 2021; 21: 4981–5013.
8. Ji C, Zhu G, Zhang C et al. Lenticular-lens-based colored antiglare dashboard surfaces. *Adv Mater Technol* 2016; 2: 1–7.
9. Clasing L, Werner-Meier D, Veldhuizen LW et al. Experimental assessment of nanoimprinted textured front-sheets for PV modules, 2022.
10. Ter Meulen JM, Veldhuizen L, Kommeren A et al. 33-6: Roll-to-plate nano-imprint lithography for high-volume production of AR glasses: equipment, materials, and processes. *SID Symp Digest Tech Pap* 2021; 52: 447–449.
11. Kordy H. Process abilities of the riblet-coating process with dual-cure lacquers. *CIRP J Manuf Sci Technol* 2015; 11: 1–9.
12. Benschop HOG, Guerin AJ, Brinkmann A et al. Drag-reducing riblets with fouling-release properties: development and testing. *Biofouling* 2018; 34: 532–544.
13. Dundar Arisoy F, Kolewe KW, Homyak B et al. Bioinspired photocatalytic shark-skin surfaces with antibacterial and antifouling activity via nanoimprint lithography. *ACS Appl Mater Interfaces* 2018; 10: 20055–20063.
14. Atthi N, Dielen M, Sripumkhai W et al. Fabrication of high aspect ratio micro-structures with superhydrophobic and oleophobic properties by using large-area roll-to-plate nanoimprint lithography. *Nanomaterials* 2021; 11: 339.
15. Dumond JJ and Yee Low H. Recent developments and design challenges in continuous roller micro- and nanoimprinting. *J Vac Sci Technol B* 2012; 30: 010801.
16. Yi P, Wu H, Zhang C et al. Roll-to-roll UV imprinting lithography for micro/nanostructures. *J Vac Sci Technol B* 2015; 33: 060801.
17. Colburn M, Grot A, Choi BJ et al. Patterning nonflat substrates with a low pressure, room temperature, imprint lithography process. *J Vac Sci Technol B: Microelectron Nanometer Struct Proce, Meas, Phenom* 2001; 19: 2162–2172.
18. Resnick DJ and Schift H. Imprint Lithography. In Smith BW and Suzuki K (eds.) *Microlithography: Science and Technology*, third ed. Boca Raton: CRC Press. ISBN 978-1-4398-7675-6, 2020. pp. 595–677.
19. Snieder J, Dielen M and van Ostayen RAJ. Simulating the residual layer thickness in roll-to-plate nanoimprinting with tensioned webs. *Micromachines* 2022; 13: 461.
20. Hooke C. The elastohydrodynamic lubrication of a cylinder on an elastomeric layer. *Wear* 1986; 111: 83–99.

21. Dowson D and Jin Z. The influence of elastic deformation upon film thickness in lubricated bearings with low elastic modulus coatings. *Tribol Ser* 1990; 17: 263–269.

22. Xue YK, Gethin DT and Lim CH. Numerical modelling of the contact between lithographic printing press rollers by soft EHL theory. *Proc Inst Mech Eng, Part J: J Eng Tribol* 1994; 208: 257–268.

23. Elsharkawy AA and Hamrock BJ. Elastohydrodynamic lubrication of elastomeric-coated surfaces in line contact. *Proce Inst Mech Eng, Part J: J Eng Tribol* 1995; 209: 119–130.

24. Taylor H. Fast simulation of pattern formation and process dependencies in roller nanoimprint lithography. *MRS Proce* 2013; 1529: 205.

25. Jain A and Bonnecaze RT. Fluid management in roll-to-roll nanoimprint lithography. *J Appl Phys* 2013; 113: 234511.

26. Coyle DJ. Forward roll coating with deformable rolls: a simple one-dimensional elastohydrodynamic model. *Chem Eng Sci* 1988; 43: 2673–2684.

27. MacPhee J, Shieh JA and Hamrock BJ. The application of elastohydrodynamic lubrication theory to the prediction of conditions existing in lithographic printing press roller nips. *Proce Twenty-first Res Conference IARIGAI* 1991; 242–276.

28. Kistler SF and Schweizer PM, (eds.) *Liquid Film Coating*. Dordrecht: Springer, Netherlands, 1997. ISBN 978-94-010-6246-6 978-94-011-5342-3. doi:10.1007/978-94-011-5342-3.

29. Grashof B and Delgado A. Analysis of influencing parameters in deformable roll coating of counter-rotating rolls. *J Coat Technol Res* 2015; 12: 63–73.

30. Habchi W. *Finite element modeling of elastohydrodynamic lubrication problems*. NJ: John Wiley & Sons: Hoboken, 2018. ISBN 978-1-119-22514-0 978-1-119-22515-7.

31. Habchi W. A numerical model for the solution of thermal elastohydrodynamic lubrication in coated circular contacts. *Tribol Int* 2014; 73: 57–68.

32. Habchi W, Eyheramendy D, Vergne P et al. Stabilized fully-coupled finite elements for elastohydrodynamic lubrication problems. *Adv Eng Softw* 2012; 46: 4–18.

33. Hamrock BJ, Schmid SR and Jacobson BO. *Fundamentals of Fluid Film Lubrication*. Second ed. Number 169 in Mechanical Engineering, New York: Marcel Dekker, 2004. ISBN 978-0-8247-5371-9.

34. Dowson D and Taylor CM. Cavitation in bearings. *Annu Rev Fluid Mech* 1979; 11: 35–65.

35. Kármán TV. *Festigkeitsprobleme im maschinenbau*. Teubner: Encyklopädie der mathematischen wissenschaften, 1910.

36. Timoshenko SP and Woinowsky-Kreiger S. *Theory of plates and shells*. Second ed. New York: McGraw-Hill Book Company, 1959. ISBN 978-0-07-064779-4.

37. Fischer A. A special Newton-type optimization method. *Optimization* 1992; 24: 269–284.

38. Bulut D, Bader N and Poll G. Cavitation and film formation in hydrodynamically lubricated parallel sliders. *Tribol Int* 2021; 162: 107113.

39. COMSOL Multiphysics® v. 6.0. COMSOL AB, Stockholm, Sweden. Available online: www.comsol.com/release/6.0. (accessed on 2021-12-15).

40. Zhao Y, Liu HC, Morales-Espejel GE et al. Effects of solid viscoelasticity on elastohydrodynamic lubrication of point contacts. *Tribol Int* 2022; 171: 107562.

41. Morphotonics Nanoimprint Technologies. Available online: https://www.morphotonics.com. (accessed on 2022-12-13).

42. Moes H. Lubrication and Beyond (Lecture Notes Code 115531). Technical report, University of Twente, Enschede, The Netherlands, 2000.

43. Marian M, Bartz M, Wartzack S et al. Non-dimensional groups, film thickness equations and correction factors for elastohydrodynamic lubrication: a review. *Lubricants* 2020; 8: 95.

44. Elrod HG. A cavitation algorithm. *J Lubr Technol* 1981; 103: 350–354.

Appendix

Notation

a_h	Hertz contact half-width (m)
d	elastomeric layer thickness (m)
$\overline{d}$	non-dimensional elastomeric layer thickness number (–)
D	bending stiffness tensioned web (Nm)
$\overline{D}$	non-dimensional bending stiffness number (–)
E	elastic modulus (Pa)
E_w	elastic modulus tensioned web (Pa)
E_eq	equivalent elastic modulus (Pa)
E'	effective elastic modulus (Pa)
F_L	effective load per unit length (N/m)
h	film/layer height (m)
h_0	rigid body displacement (m)
h_f	final film/layer height (m)
h_w	initial web height (m)
H	dimensionless film/layer height (–)
H_0	dimensionless rigid body displacement (–)
H_f	dimensionless final film/layer height (–)
H_w	dimensionless initial web height (–)
g	gap between elastomeric layer and tensioned web (m)
g_0	initial gap between elastomeric layer and tensioned web (m)
G	dimensionless gap between elastomeric layer and tensioned web (–)
G_0	dimensionless initial gap between elastomeric layer and tensioned web (–)
K	dimensionless curvature of tensioned web (–)
$\overline{M}$	non-dimensional modified load number (–)
p	hydrodynamic film pressure (Reynolds) (Pa)
p_c	tensioned web contact pressure (Pa)
p_n	normal stress acting on tensioned web (Pa)
p_h	Hertz contact pressure (Pa)
P	dimensionless hydrodynamic film pressure (Reynolds) (–)
P_c	dimensionless tensioned web contact pressure (–)
P_n	dimensionless normal stress acting on tensioned web (–)
R	roller radius (m)
T	web tension (N/m)
$\overline{T}$	non-dimensional web tension number (–)
t	tensioned web thickness (m)
u	elastic deformation in x' (m)
u_1	roller surface imprint velocity (m/s)
u_2	substrate surface imprint velocity (m/s)
u_Σ	sum of velocities u_1 and u_2 (m/s)

U	dimensionless elastic deformation in X' (–)		Z_w	dimensionless web height profile (–)
$\overline{U}$	non-dimensional speed number (–)		η	resin dynamic viscosity (Pas)
w	elastic deformation in z' (m)		κ	curvature of the tensioned web (1/m)
w_w	tensioned web deformation in z' (m)		λ	Lamé's first parameter (–)
W	dimensionless elastic deformation in Z' (–)		μ	Lamé's second parameter (–)
$\overline{W}$	non-dimensional load number (–)		ν	Poisson's ratio (–)
W_w	dimensionless tensioned web deformation in Z' (–)		ν_w	Poisson's ratio tensioned web (–)
x	space coordinate in horizontal direction (m)		σ_n	normal component of the stress tensor (–)
x'	space coordinate tangential to roller surface (m)		σ_t	tangential component of the stress tensor (–)
X'	dimensionless space coordinate tangential to roller surface (–)		Ω	computational domain
			Ω_T	top boundary
z	space coordinate in vertical direction (m)		Ω_L	left boundary
z'	space coordinate normal to roller surface (m)		Ω_R	right boundary
z_w	web height profile (m)		Ω_C	contact pressure boundary
Z'	dimensionless space coordinate normal to roller surface (–)		Ω_H	hydrodynamic lubrication boundary